

Article

Fused Filament Fabrication of Thermal-Shock-Resistant Fine-Grained Refractories for Steel-Casting Applications

Serhii Yaroshevskiy^{1,*}, Piotr Malczyk¹, Christian Weigelt¹, Jana Hubalkova¹ , Steffen Dudczig¹, Uwe Lohse² and Christos G. Aneziris¹

¹ Institute of Ceramics, Refractories and Composite Materials, TU Bergakademie Freiberg, Agricolastr. 17, 09599 Freiberg, Germany

² XERION BERLIN LABORATORIES@GmbH, Gross-Berliner Damm 84 A, 12487 Berlin, Germany

* Correspondence: serhii.yaroshevskiy@ikfww.tu-freiberg.de; Tel.: +49-37-3139-3626

Abstract: Three-dimensionally printed fine-grained refractory ceramics ready for use in contact with liquid steel based on developed one-step thermal debindable ceramic filaments that do not require any chemical solvent pre-debinding are investigated. This work exhibits the most favourable debinding and sintering regimes with an excellent form stability and reproducibility of printed products ensured. The structure of the sintered products was examined with computed tomography. The designed inner geometry with micro-porosity introduced during debinding combined with pre-designed printed macro-cavities enabled the outstanding thermal-shock performance of the specimens. The functionality of the sintered refractory products in the form of casting nozzles was preliminarily tested in contact with steel melt using a hot-stage microscope. The structure of the specimen was subsequently examined with laser scanning microscopy and scanning electron microscopy. The mechanical properties of printed samples were studied via mercury intrusion porosimetry, compressive strength testing, and spatial tensile strength testing. According to the results, the cold crushing strength of the 3D-printed specimens in the printing direction was comparable to that of pressed fine-grained alumina specimens (50–60 MPa). The measured porosity was 21.5 vol% with a pore size less than 10 μm , which is suitable for applications in contact with molten steel. In order to show thermal-shock resistance of the 3D-printed casting nozzle, a 100 kg steel-melt flow test was performed in a steel-casting simulator with the nozzle surviving all related thermal shocks as well as the ferrostatic pressure of the melt. The evaluated composition and production route of the filaments can be utilized to produce one-step, thermally debindable, thermal-shock-resistant refractory parts with a complex inner structure that are applicable in an industrial environment.

Keywords: additive manufacturing; fine-grained refractories; fused filament fabrication; thermal-shock resistance



Citation: Yaroshevskiy, S.; Malczyk, P.; Weigelt, C.; Hubalkova, J.; Dudczig, S.; Lohse, U.; Aneziris, C.G. Fused Filament Fabrication of Thermal-Shock-Resistant Fine-Grained Refractories for Steel-Casting Applications. *Ceramics* **2023**, *6*, 475–491. <https://doi.org/10.3390/ceramics6010027>

Academic Editors: Frederic Monteverde and Antonio Riveiro

Received: 16 December 2022

Revised: 17 January 2023

Accepted: 2 February 2023

Published: 7 February 2023



Copyright: © 2023 by the authors. Licensee MDPI, Basel, Switzerland. This article is an open access article distributed under the terms and conditions of the Creative Commons Attribution (CC BY) license (<https://creativecommons.org/licenses/by/4.0/>).

1. Introduction

Ceramic refractory materials are exposed to very high thermal gradients and rapid temperature changes that cause thermal stresses. Usually, in order to withstand such stresses, refractory products are produced using coarse-grained ceramics. The critical gradient for fine-grained (grain sizes less than 100 μm) alumina is approx. 200 K, which is insufficient for refractory application. However, the drawback of coarse-grained material is its open porosity and thus the possibility of infiltration of steel in between the grains, which meaningfully lowers the lifespan of the refractory material [1]. Especially for continuous steel-casting applications, carbon-bonded refractories are applied as nozzles in order to withstand the extreme thermal shock attack [2]. Thereby, carbon-containing refractories interact with the steel melt at elevated temperatures and clogging phenomena via carboth-ermal reactions lead to critical changes in the flowing properties through the nozzles, which can cause the interruption of the casting process [3,4]. Furthermore, in order to protect the

carbon against oxidation, glazes are applied, which have a negative impact on the steel's properties and can cause inclusions in the steel product [5–7].

The ability of the bodies to withstand the thermal stresses can be described by the so-called thermal stress resistance parameters (TSR parameters): R , R' , R'' , R''' , and R_{st} . These parameters take into consideration the material properties and conditions of heat transfer [8,9]. The thermal stress damage resistance parameter R''' represents the resistance to crack propagation of already-existing small defects. High values of R''' reflect a relatively good resistance of the refractory material against crack propagation under thermal-shock loading, and hence, better thermal stress resistance [10,11].

R''' is proportional to the modulus of elasticity E [MPa] and specific fracture energy G_f [J/m] and inversely proportional to the squared fracture strength σ^2 [MPa²]. According to Skiera et. al. [10], who compared the R''' parameter for alumina-based refractory (A) to the respective parameter of alumina-based refractory with titania and zirconia additives (AZT), the latter showed almost ten times higher values of R''' — 8.39 ± 2 mm against 0.85 ± 0.05 mm—despite the higher specific fracture energy of the first.

Habib et. al. showed [12] that a combination of fine-grained alumina refractory powders with a flame-spraying technique that incorporates layer-by-layer microstructure design achieves a higher thermal-shock performance. Moreover, such a flame-sprayed layer-by-layer structure introduces micro-crack network patterns, which lead to dissipation of the major crack propagation energy [6,13].

Therefore, it is possible to produce fine-grained ceramic refractories without any carbon doping by means of a layer-by-layer structure of the produced part. Such a structure could be introduced with an additive manufacturing technique. Furthermore, the application of additive manufacturing techniques enables the introduction of any pre-designed inner geometry, preserving a considerably high final density of the product, which increases the specific fracture energy and thus improves the thermal-shock resistance of the produced part.

Additive manufacturing (AM) is a promising, continuously developing technology that enables the cost-efficient fabrication of tailor-made products with sophisticated shapes. The main routes of AM production in the field of ceramics are powder-based techniques and suspension-based techniques. The first is based on the powder bed and therefore lacks compaction, which leads to a lower density of the green body and thus is not suitable to produce components with dense microstructure and relatively low surface roughness [14]. The most common suspension-based techniques are lithography-based ceramic manufacturing (LCM) [15], fused filament fabrication (FFF), and thermoplastic 3D printing (T3DP) [16].

FFF and T3DP utilize a thermoplastic binder, in contrast to the photo-curing polymers used in LCM. This not only enables the use of powders with any optical properties without any adjustments to the binder system, but also decreases the investment costs in the equipment because FFF and T3DP printers are well-developed for plastic and metal applications and a variety of devices is available. This paper focuses on the FFF technique, where material in the form of a plastic filament is printed by melting through a nozzle, forming the three-dimensional product body layer-by-layer [17,18]. Such a technique, among the other AM advantages, facilitates the implementation of more than one material to be sintered simultaneously, enabling the development of multi-material designs [19].

The application of FFF techniques allows to manufacture thin-walled, fine-grained refractories with a pre-defined hollow inner structure and a dense, fine-grained, layered outer structure at the same time [20]. The dense, fine-grained, layer-by-layer outer structure not only contributes to a high corrosion and infiltration resistance, which are indispensable for industrial metallurgical applications, but also, due to the thin-walled layer-by-layer structure with fine pores and the functional geometry of the ceramic component (macro-cavities in between the inner and outer layers), leads to a sufficient decrease in the crack-propagation energy, as has been explored in thermal-spraying-generated structures [6,21]. Moreover, the thermal debinding process introduces additional micro-cracks and voids into the body of FFF-manufactured products, which are also known to be advantageous to

the thermal-shock performance of ceramic refractory materials [22,23]. These voids, formed during the evaporation of the thermoplastic phase of the printed material, inhibit the crack propagation during thermal shock further. As a function of the binder amount and the grain size distribution of the ceramic material these pores can be tailored and with the aid of FFF positioned in high-thermal-stress areas of the ceramic component.

The application of the “Fusion Factory” FFF 3D printer (developed at XERION BERLIN LABORATORIES, Berlin) for the manufacture of complex functional refractory products requires the utilization of printable filaments. The filaments comprise two components: solid material and a suitable binder. The solid material is a material desired to be sintered as a final product, whereas the binder is a polymer-based mixture ensuring the flexibility of the filament and facilitating the printing [24,25]. Such a binder possesses thermoplastic characteristics with a melting temperature of 90–200 °C depending on the type of polymer used.

Due to the variability in form and shape of the produced parts, combined with the relative simplicity and low price, the FFF method has been investigated by many research groups over recent years. The main focus of such research was filament preparation, printability [26–30], and, more seldom, the evaluation of the mechanical properties [31] or inner structure of printed parts [32].

This work is focused on the preparation of the full production chain of the filament material and the evaluation of suitable thermal treatments and printing parameters. Elaborated filaments were characterized and used to produce refractory parts (using steel-casting nozzles as an example) whose mechanical and thermo-mechanical properties were evaluated. The inner geometry was designed and implemented in order to increase the thermal-shock resistance of the parts. As a proof of the industrial applicability of parts produced with the FFF method, the printed nozzles underwent testing in a steel-casting simulator.

2. Materials and Methods

As a solid material for filaments, AR78 Almatiss[®] magnesia-rich alumina spinel (Almatiss, Ludwigshafen, Germany) was selected. The spinel powder particle size should not exceed 20 µm, since larger particles might clog the extruding nozzle during filament manufacturing.

In order to obtain a sufficient amount of solid material in the filament and preserve its substantial flexibility, the filaments were produced with 52 vol% of solid material, the rest being the binder–plasticizer mixture. This mixture was based on polyethylene Rowalit H150 with the addition of Rowalit H70 (Rowak, Klettgau-Griessen, Germany) to achieve a melt flow index (which is described in ISO 1133-1:2011) of the polyethylene at 190 °C of 100.

Numerous different binder additives were used to optimize the filament behaviour under increasing temperatures. Here, inter alia, stearic acid ($\geq 98\%$, Carl Roth, Karlsruhe, Germany), cellulose powder (Sigma-Aldrich, Taufkirchen, Germany), methylcellulose (Sigma-Aldrich, Taufkirchen, Germany), and lignin sulfonate (C12C, Otto Dille, Norderstedt, Germany) were applied. Stearic acid was used as a lubricant facilitating the filament-extrusion process. The cellulose, methylcellulose, and lignin sulfonate were applied to ensure the printability of the filament, sufficient strength during the printing process, and its high form stability at elevated temperatures. The most favourable binder system was composed of a polyethylene base with additions of stearic acid, lignin sulfonate, and cellulose, with their exact content depending from the applied solid material. Filaments containing 52 vol% AR78, 35.52 vol% polyethylene, 4.8 vol% stearic acid, 4.8 vol% cellulose, and 2.88 vol% lignin sulfonate were labelled 3D-AR78.

Prior to the filament extrusion, the solid material/binder mixture was prepared using the Eirich[®] laboratory mixer EL-1 (Maschinenfabrik Gustav Eirich, Hardheim, Germany). The solid material was mixed with the binder for 180 s at 2500 rpm, after which it was extruded using a Brabender[®] twin-screw extruder (Brabender GmbH & Co., Duisburg, Germany) at 128 °C and a torque of 90 Nm. The filament extrusion consisted of four con-

secutive extrusion steps ensuring excellent filament homogeneity and consistent filament properties. After each extrusion the filament was fragmented with scissors into small pieces of 10 mm and used as a feedstock material for subsequent extrusion. During the final extrusion, the filament was wound onto a spool with a semi-automatized winding rig developed for this purpose and attached to the extruder as shown in Figure 1.

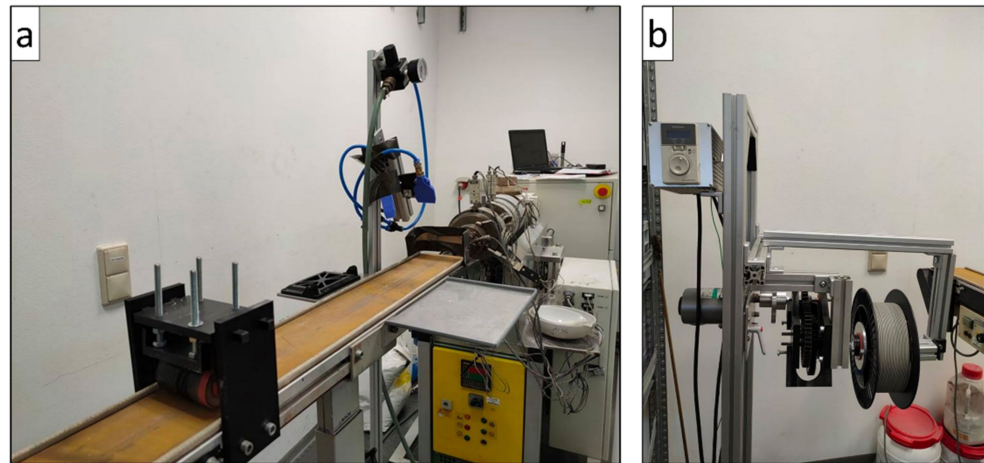


Figure 1. Extrusion setup: (a) Brabender® twin-screw extruder, (b) semi-automatized winding device.

The diameter of the extruded filaments was set to be $2.85 \text{ mm} \pm 0.1 \text{ mm}$ (Figure 2a), since such a diameter is commonly used for 3D printers. All manufactured filaments were tested for geometrical stability. During this test, filament samples of length 60 mm were placed on inert alumina bricks with gaps between them of 25 mm (Figure 2b) and heated to temperatures of up to $400 \text{ }^\circ\text{C}$ in air for 2 h, matching the temperature range of the debinding process. Afterwards, the deflection as well as changes in diameter were determined and mutually compared in order to find the most stable filament composition at elevated temperatures.

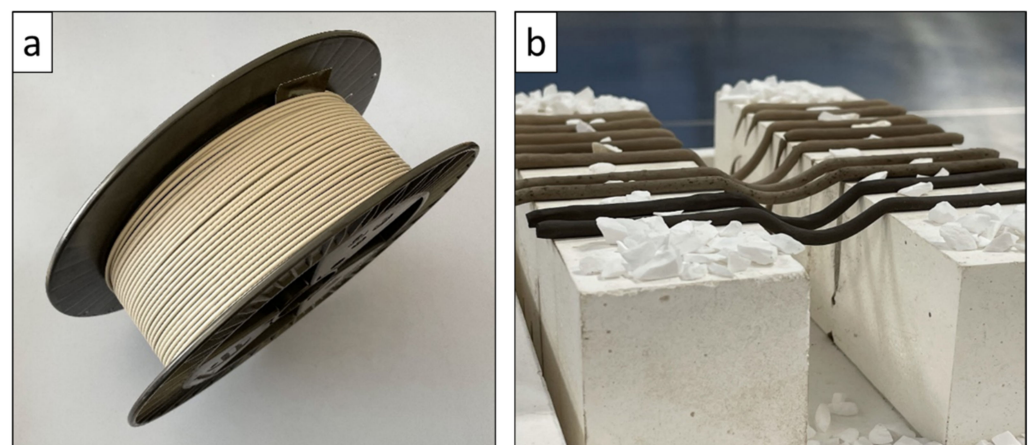


Figure 2. Produced filaments: (a) rolled ready-to-print filaments, (b) thermal stability test setup.

Due to the relatively high content of solid material (52 vol%), the extruded filaments were insufficiently flexible for the 3D-printing process at room temperature. However, due to the thermoplastic behaviour of the polyethylene, the flexibility of the filaments increases with the temperature of the environment. The radii of curvature of the prepared ceramic filament at different temperatures can be seen in Figure 3. As illustrated in Table 1, the highest flexibility occurred at $60 \text{ }^\circ\text{C}$; therefore, this temperature was set as the temperature of the printing chamber.

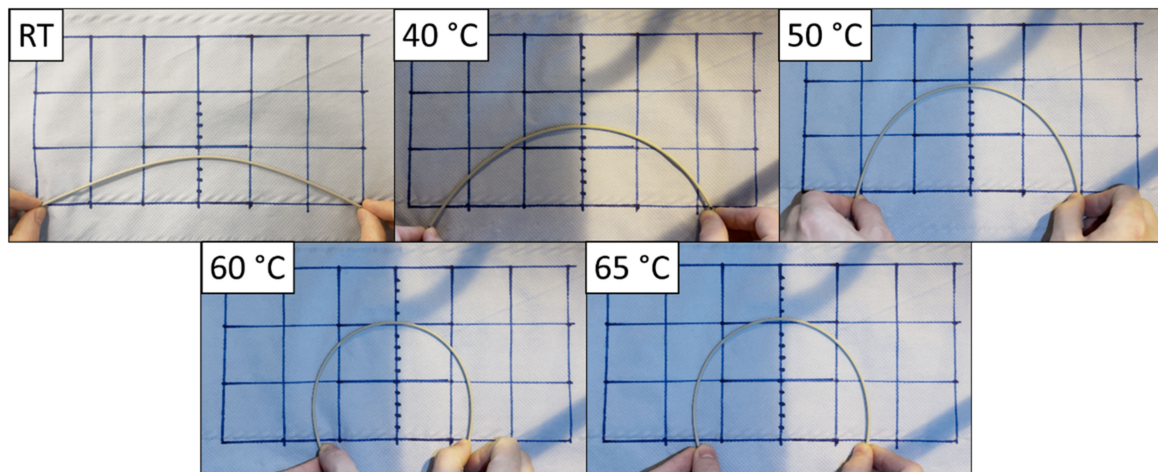


Figure 3. Flexibility test of manufactured 3D-AR78 filaments at different temperatures.

Table 1. Estimated radii of filaments prior to breaking depending on the temperature.

Temperature in °C	Room Temperature	40	50	60	65
Radius of maximum curvature, mm	158	97	79	60	61

All printing parameters of the XERION® Fusion Factory 3D printer (Figure 4a) used for the production of the samples are listed in Table 2.

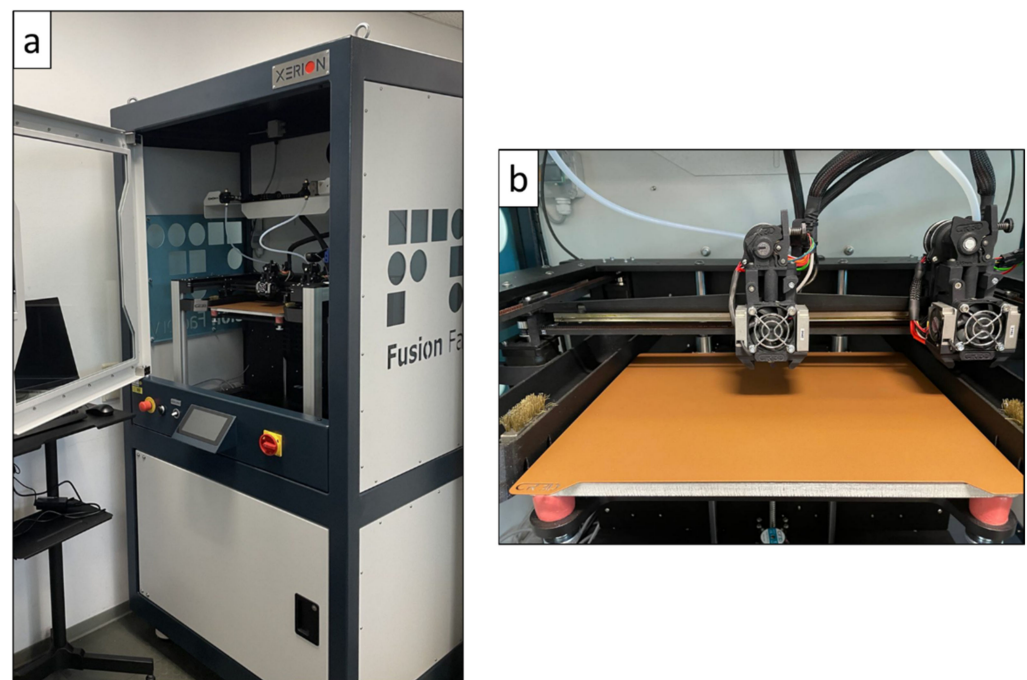


Figure 4. Printing setup: (a) XERION® Fusion Factory 3D printer setup, (b) preheatable printing chamber.

Table 2. Printing parameters of the XERION[®] Fusion Factory 3D printer.

Parameter	Value
Diameter of the printing nozzle	0.8 mm
Layer width	0.65 mm
Layer height	0.3 mm
Top layers	3
Bottom layers	3
Perimeter	1
Infill	25%
Infill pattern	+/-45°
Printing nozzle temperature	180 °C
Printing bed temperature	50 °C
Printing chamber temperature	approx. 60 °C
Printing speed	20 mm/s

The printed casting nozzles (Figure 5) had an initial diameter of approx. 30 mm and a height of approx. 33 mm. The printing was carried out with 25% infill with a 45° pattern introducing the controlled hollow body of the structure. The inner and outer walls of the casting nozzles were 2 mm thick. The temperature of the bed was set to 50 °C in order that the printed body attaches to the bed surface during the printing process. The temperature of the printing chamber was set to 60 °C and the temperature of the printing nozzle of a printing head to 180 °C.

**Figure 5.** 3D-AR78-based nozzles: (a) as printed, (b) debound, (c) sintered.

After printing, numerous debinding and sintering treatment regimes were designed and tested in order to achieve sufficient stability of the debound nozzle, so that the debound sample would be transportable to the sintering oven.

Due to the complex geometry of steel-casting nozzles, a series of additional samples was printed and utilized for mechanical characterization, i.e., cold compressive strength testing, splitting tensile strength testing, and mercury porosimetry measurements. For the compressive strength and splitting tensile strength tests, layered hollow cylinders in a simplified form were printed with the same 3D-AR78-based filament material and printing parameters as for the steel-casting nozzles. The outer diameter of the cylinders was 15 mm, height 15 mm, and wall thickness 2.5 mm (Figure 6). Such a layer-by-layer structure complies with the structure of the steel-casting nozzles. For the mercury porosimetry test, a set of bulk cylinders (without macro-cavities) with a diameter and height of 5 mm were printed. All printed cylinders were debound and sintered with thermal treatment regimes designed for nozzles.

Compressive strength testing was performed vertically in order to test strength in direction of printing with a TIRAtest 2850 machine (TIRA GmbH, Schalkau, Germany) with a loading cell of 20 kN and a loading rate 2 mm·min⁻¹, according to DIN EN 993-5 (Figure 7a). Splitting tensile strength testing was performed horizontally in order to simulate the fracture load in the direction perpendicular to printing with the fracture load in the direction of printing. This test was performed with a TIRAtest 2420 machine (TIRA

GmbH, Schalkau, Germany) with a loading cell of 1 kN and a loading rate of $2 \text{ mm} \cdot \text{min}^{-1}$, according to DIN EN 12390-6 (Figure 7b).



Figure 6. 3D-printed cylinders for compression and splitting tensile tests in green state.

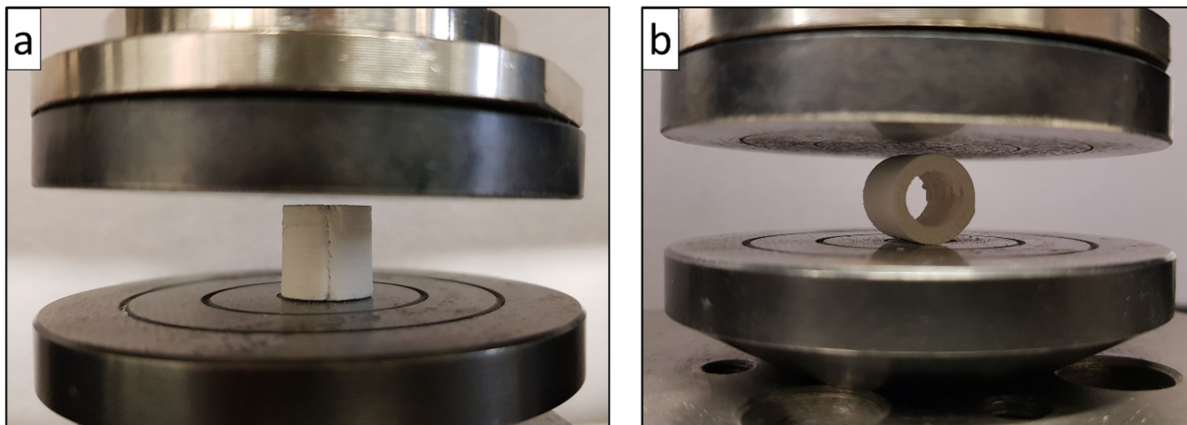


Figure 7. Mechanical tests: (a) compressive strength test setup, (b) splitting tensile test setup.

Mercury porosimetry tests were carried out to evaluate the open porosity and particularly the pore size distribution of the printed samples. The measurements were conducted in a pressure range of up to 420 MPa with an AutoPore V 9600 (Micromeritics Instrument Corp., Norcross, GA, USA) in accordance with DIN ISO 15901-1.

In order to estimate the industrial applicability of the 3D-printed components, the sintered nozzles based on the AR78 spinel were subjected to thermal-shock testing. The sintered nozzles were slowly heated up to $850 \text{ }^\circ\text{C}$ with a heating rate of 5 K/min , held for 30 min at $850 \text{ }^\circ\text{C}$, and subsequently underwent a sudden thermal shock with pressurized air (1.2 bar). The compressive strength of the nozzles before and after quenching was measured according to DIN EN 51104 with a compression speed of 2 mm/min and a maximum force of 5 kN in the universal TIRAtest 2850 (TIRA GmbH, Schalkau, Germany). In order to compensate for surface irregularities of the sintered 3D-printed nozzles, a foam rubber pad with a thickness of 4 mm was placed underneath the nozzle.

To visualize the inner 3D structure and potential faults, computed tomography using CT-ALPHA (ProCon X-ray GmbH, Garbsen, Germany) was used on sintered and thermal-shocked specimens (with a voltage set to 150 kV and a current of $60 \text{ } \mu\text{A}$).

The sintered steel-casting nozzles were intended for the static corrosion test in contact with a steel-melt alloy. This test was performed in a hot-stage microscope (STM, Raczek, Garbsen, Germany) (Figure 8). The specimen was fixed inside a corundum crucible with a prism of 316L stainless steel inside the nozzle. The steel in the nozzle was molten under a continuous argon purging atmosphere (O_2 content $< 5 \text{ ppm}$) at $1600 \text{ }^\circ\text{C}$ with a heating

rate of 10 K/min. The holding time at this temperature was 2 h. After the experiment, the internal surface of the nozzle, which stayed in contact with the steel, was analyzed with a Philips XC-30 scanning electron microscope (Keyence, Itasca, IL, USA).

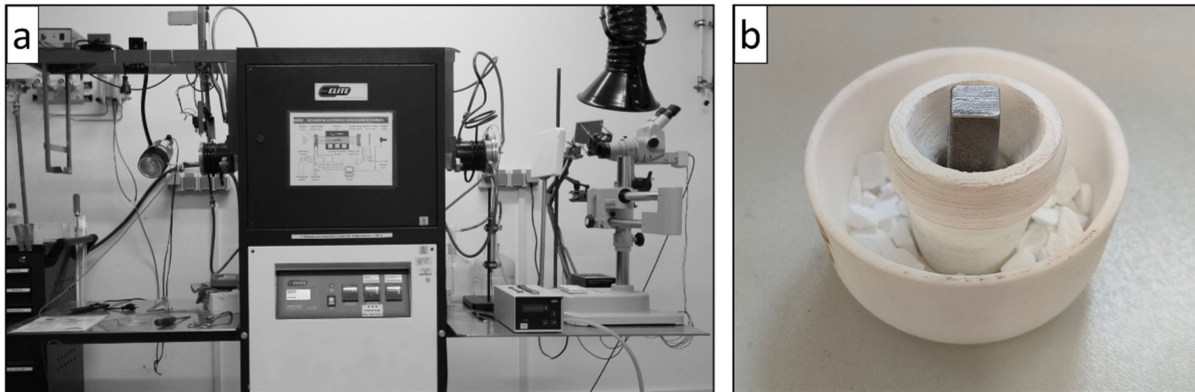


Figure 8. Hot-stage microscope setup: (a) general view, (b) measuring setup.

Finally, the steel-melt flow test was performed under semi-industrial conditions with a steel-casting simulator (Systec Gruppe, Systec Vacuum Systems, Kalstadt/Main, Germany) [33]. For this purpose, the refractory nozzle was fixed in the chamber using the ceramic glue Keratin K (Rath, Meissen, Germany) in a special refractory tundish component with only one nozzle path (Figure 9). After the preheating to 800 °C of the whole system, approx. 100 kg of molten steel 42CrMo4 at 1600 °C was poured through the nozzle by inclining the crucible as shown in Figure 9a.

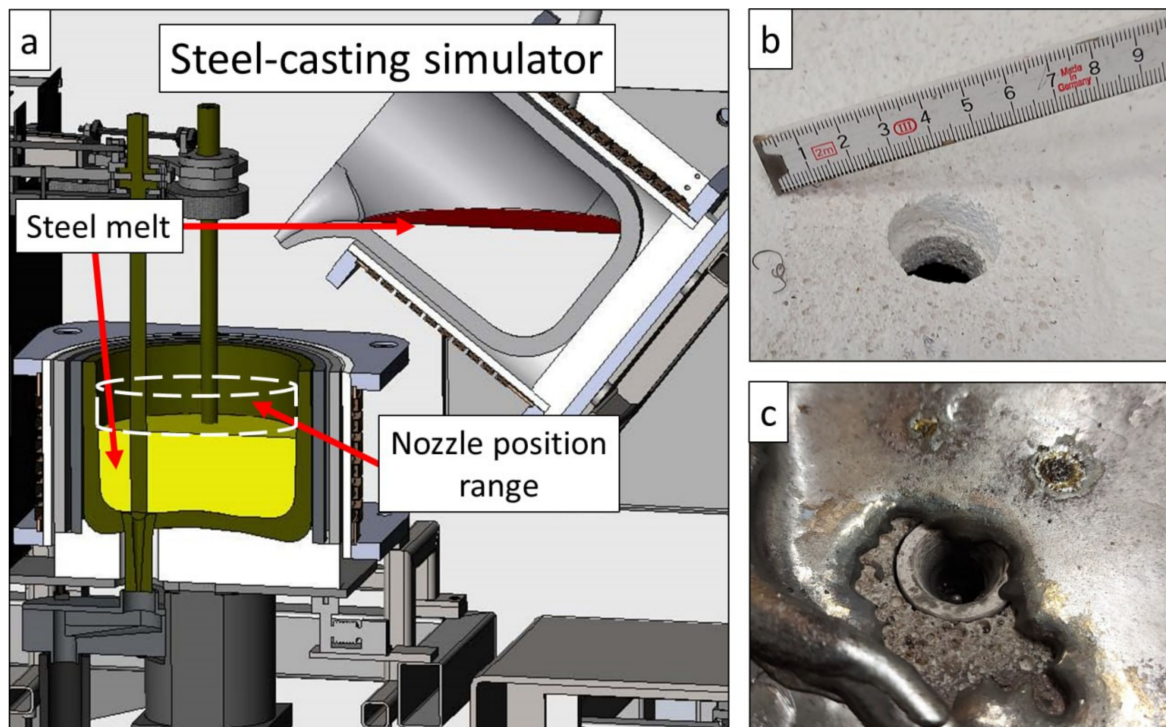


Figure 9. Steel-casting simulator: (a) casting setup, (b) nozzle holder before casting, (c) nozzle after casting 100 kg of steel melt.

After steel-melt casting, the removed nozzle underwent computed tomography analysis in order to investigate crack propagation and possible infiltration of steel. The reconstructed voxel size of this nozzle was 27.5 μm . Micro-cracks larger than 30 μm before and after the steel-casting tests can be evaluated.

3. Results and Discussion

3.1. Filament Manufacture

The final elaborated filament composition, based on the Almatiss[®] AR78 alumina-rich magnesium aluminate spinel (MgAl_2O_4) solid material, and its detailed binder–plasticizer composition are listed in Table 3.

Table 3. Composition of 3D-AR78 filament systems.

	Solid Material 52 vol%	AR78 Spinel	Almatiss [®] Spinel AR78
3D-AR78	Binder–plasticizer mixture 48 vol%	Stearic acid	4.80 vol%
		Lignin sulfonate	2.88 vol%
		Cellulose powder	4.80 vol%
		Polyethylene	35.52 vol%

The 3D-AR78 filament material composition fulfilled our requirements for stability during the thermal treatment.

3.2. Debinding and Sintering Thermal Treatments

DCS/TG analysis of the filament material 3D-AR78 was explored in air atmosphere with a heating rate of $10 \text{ K}\cdot\text{min}^{-1}$ (STA 409 PC Luxx, Netzsch, Germany). The key points of interest are an endothermic peak with a peak maximum of 105°C with an offset point at approx. 95°C , an exothermic peak with a peak maximum of 210°C with an offset point at approx. 180°C , and paired exothermic peaks with peak maxima 395°C and 445°C (Figure 10). The first two peaks represent polymer transformation processes, which are indicated by no change in mass of the tested material and considerable changes in heat flow [34,35]. The second two peaks have an offset point at approx. 300°C , which indicates the start of an active removal phase and a rapid loss of mass due to polymer evaporation.

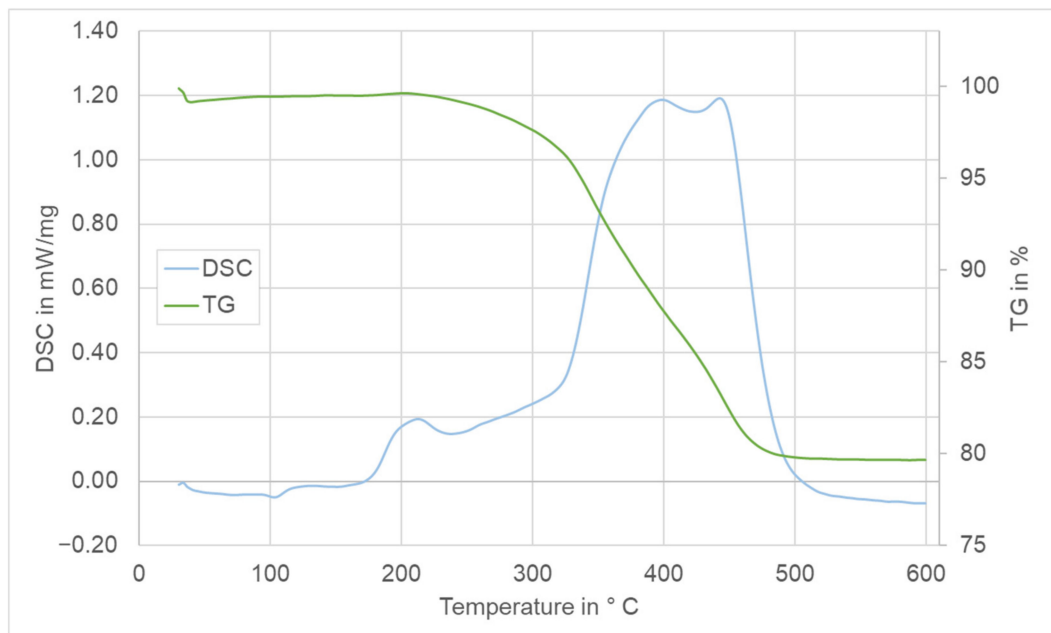


Figure 10. DSC/TG analysis of 3D-AR78 filament material.

Polyethylene, which is used as the main thermoplastic material of this composite, has a melting point at approx. 100°C . Therefore, it is expedient to have a rapid heating from this temperature up to an offset point of the next polymer transformation, when the material starts to lose its thermoplastic characteristics with a further loss of mass. Thus, the

heating rate between 90 °C and 220 °C was set to 300 K/h. Three intermediate plateaus of thermal debinding—at 220 °C, 320 °C, and 380 °C—are the respective offset points of the subsequent polymer transformations. In order to ensure full debinding of each polymer component at given temperatures, the holding time at each of these temperature points was set to 4 h. Moreover, to ensure sufficient form stability prior to sintering, it is indispensable for the samples to maintain some amount of binder after the debinding process. Therefore, the final debinding temperature was set to 380 °C. All nozzles were thermally debound up to 380 °C for approx. 30 h without any solvent-based pre-debinding step. By holding at this temperature, the mass loss of filaments during preliminary testing was approx. 18 mass%; thus, debound products lost approx. 90% of the binder, as shown in Table 4.

Table 4. Mass loss of the filaments after thermal debinding treatment.

Filament	Initial Mass	Mass after Debinding	Mass Loss
1	1.491 g	1.225 g	17.84%
2	1.498 g	1.230 g	17.87%
3	1.486 g	1.204 g	18.98%
4	1.482 g	1.216 g	17.95%
5	1.476 g	1.204 g	18.43%

The exact debinding parameters, elaborated with DCS/TG analysis as well as numerous preliminary tests, are presented in Table 5. The subsequent sintering of the nozzles was designed to slowly finish the debinding process via step-by-step heating of the bodies to 600 °C followed by sintering at 1600 °C. The sintering process in total lasted approx. 109 h; its exact parameters are presented in Table 6. Through the debinding process, the nozzles lost approximately 15 mass%. The sintering-related shrinkage was approx. 7% in the height and approx. 10.5% in the diameter direction. All surfaces as well as the designed infill structure of the nozzles remained undistorted.

Table 5. Debinding thermal treatment regime.

	Starting Temperature	Heating Rate	Ending Temperature	Holding Time
Step 1	20 °C	60 K/h	90 °C	5 min
Step 2	90 °C	300 K/h	220 °C	4 h
Step 3	220 °C	60 K/h	320 °C	4 h
Step 4	320 °C	30 K/h	380 °C	4 h
Step 5	380 °C	−30 K/h	20 °C	0 min

Table 6. Sintering thermal treatment regime.

	Starting Temperature	Heating Rate	Ending Temperature	Holding Time
Step 1	20 °C	30 K/h	330 °C	1 h
Step 2	330 °C	6 K/h	450 °C	2 h
Step 3	450 °C	6 K/h	500 °C	4 h
Step 4	500 °C	6 K/h	600 °C	0 min
Step 5	600 °C	60 K/h	1600 °C	4 h
Step 6	1600 °C	−60 K/h	20 °C	0 min

The evaluation of nozzle quality after sintering was performed with computed tomography, as shown in Figure 11. The achieved nozzle quality without any cracks larger than 30 µm is suitable for steel-casting applications.

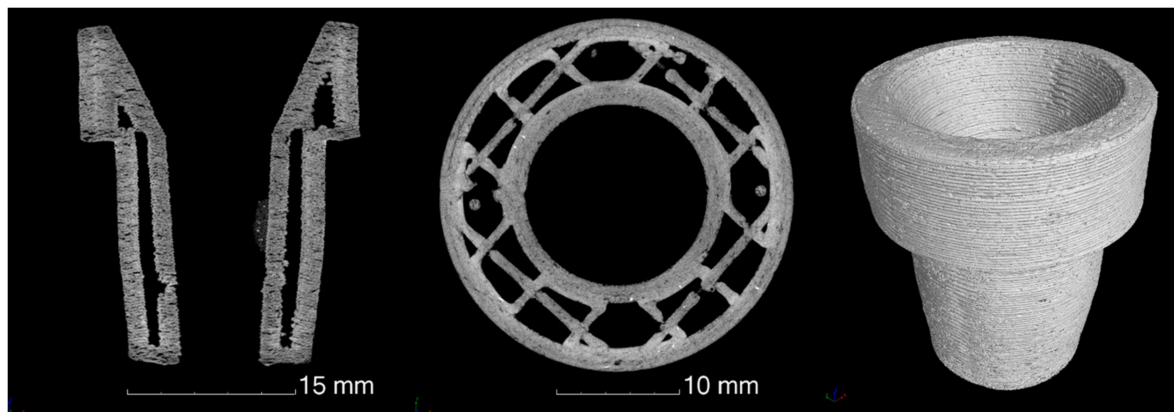


Figure 11. Computed tomographic images of the sintered nozzle from 3D-AR78-based material: reconstructed vertical 2D slice (left) and horizontal 2D slice (middle) as well as 3D-rendered (right).

3.3. Mechanical Tests

Nötzel et al. compared the debindability and printability of Al_2O_3 filaments based on polyvinylbutyral (PVB) as the backbone polymer and polyethyleneglycol (PEG) as the low-molecular-mass component with a 50 vol.% ceramic load to wax/polyethylene-based Al_2O_3 filaments. According to them [36], the average shrinkage of the first was approx. 20.75%, and of the latter, in the range of 18–20.5% for dense bodies, which is considerably higher than the shrinkage achieved with the polyethylene–cellulose–lignin–sulfonate-based composition that is being discussed. Moreover, wax/polyethylene filaments required a solvent-based pre-debinding step prior to thermal debinding, whereas PEG/PVP filaments required pre-debinding in cold water. Filaments based on the polyethylene–cellulose–lignin–sulfonate system, according to the presented results, are a suitable alternative to established ones.

The results of the compressive strength tests are presented in Table 7.

Table 7. Results of compressive strength tests.

Specimen	Fracture Load	Compressive Stress	Inner Diameter	Outer Diameter
1	2361.6 N	31.18 MPa	7.49 mm	12.35 mm
2	3060.9 N	46.32 MPa	8.21 mm	12.31 mm
3	4331.9 N	54.24 MPa	7.90 mm	12.81 mm
4	4956.4 N	73.86 MPa	8.16 mm	12.33 mm
5	5221.8 N	76.18 MPa	8.35 mm	12.53 mm
6	3218.4 N	42.90 MPa	8.11 mm	12.70 mm
Mean value	3858.5 N	54.11 MPa	8.04 mm	12.51 mm
St. dev.	1146.7 N	17.83 MPa	0.31 mm	0.21 mm

According to Schafföner et. al. [37], for coarse-grained alumina pressed at 50 MPa, cold crushing strength values are in the range of 52–74 MPa, which is comparable to the results achieved by fine-grained printed and sintered hollow cylinders. High values of mechanical strength in the printing direction are indispensable for the utilization of parts produced via 3D printing for applications with molten steel. Moreover, as was studied by Lube et. al. [38], the layered structure of the manufactured bodies allows an increase in the resistance to crack propagation as well as mechanical reliability.

Splitting tensile strength tests are commonly used for the characterization of concrete; however, such a test was conducted on printed specimens in order to compare the fracture load in the direction perpendicular to printing with the fracture load during the cold crushing strength test. The results of the splitting tensile tests are shown in Table 8:

Table 8. Results of splitting tensile strength tests.

Specimen	Fracture Load	Inner Diameter	Outer Diameter
1	273.49 N	7.77 mm	12.77 mm
2	177.74 N	8.12 mm	12.77 mm
3	129.43 N	8.29 mm	12.31 mm
4	267.07 N	7.81 mm	12.72 mm
5	277.73 N	7.84 mm	12.67 mm
6	181.69 N	8.28 mm	12.39 mm
Mean value	217.86 N	8.02 mm	12.61 mm
St. dev.	62.99 N	0.24 mm	0.20 mm

Obviously, in the direction perpendicular to the printing direction, hollow cylinders showed much lower values of fracture load, and since the cylinders were hollow, following the structure of refractory nozzles, there is no standardized approach to determine the splitting tensile strength.

3.4. Thermal-Shock Test

Sintered nozzles underwent thermal-shock tests using air quenching from 850 °C to room temperature. No visible cracks or failures after the thermal shocking were observed. However, the fracture load of the quenched nozzles decreased by approximately 26% from 1685 kN in the sintered state to 1239 kN in the quenched state. The structure of the nozzles after the thermal shocking was examined with computed tomography and compared to the nozzles in a sintered state, as shown in Figure 12.

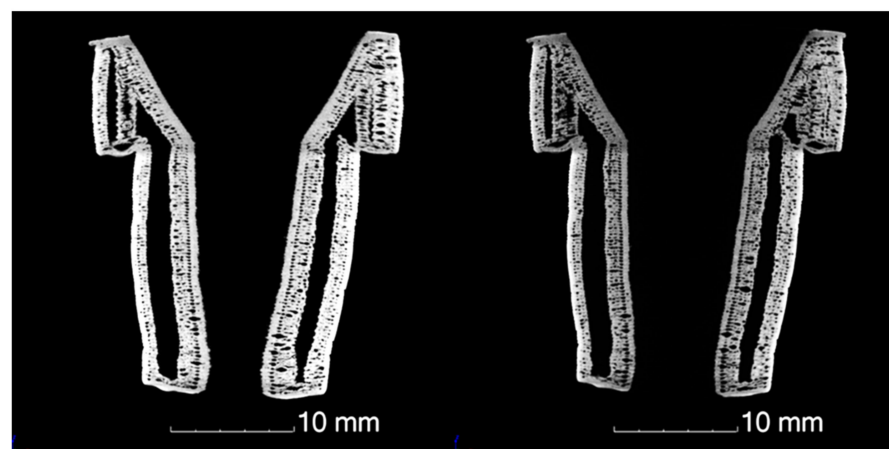


Figure 12. Reconstructed 2D-CT slices of sintered refractory before (left) and after (right) a thermal-shock test.

No initiation of new micro-cracks or propagation of pre-existing micro-cracks were identified with computed tomography. Therefore, it is assumed that the potentially initiated new micro-cracks were less than 30 μm , since the reconstructed voxel size of the nozzle was 27.5 μm .

3.5. Mercury Intrusion Porosimetry

The open porosity of full 3D-printed cylinders determined with mercury intrusion porosimetry was 21.5 vol%. There is a trimodal distribution of pore sizes (Figure 13). The pore size peaks at 7 nm, 4.22 μm , and 9.81 μm . The peak at 9–10 μm is split, because at this pressure range (between atmospheric pressure 0.1035 MPa and 0.2 MPa), a transposition of the penetrometer from the low-pressure station to the high-pressure station is necessary. Applications of ceramics/refractories in the steel industry require pore sizes less than 30 μm in order to avoid a steel-melt infiltration in a non-wetting material such as spinel [39].

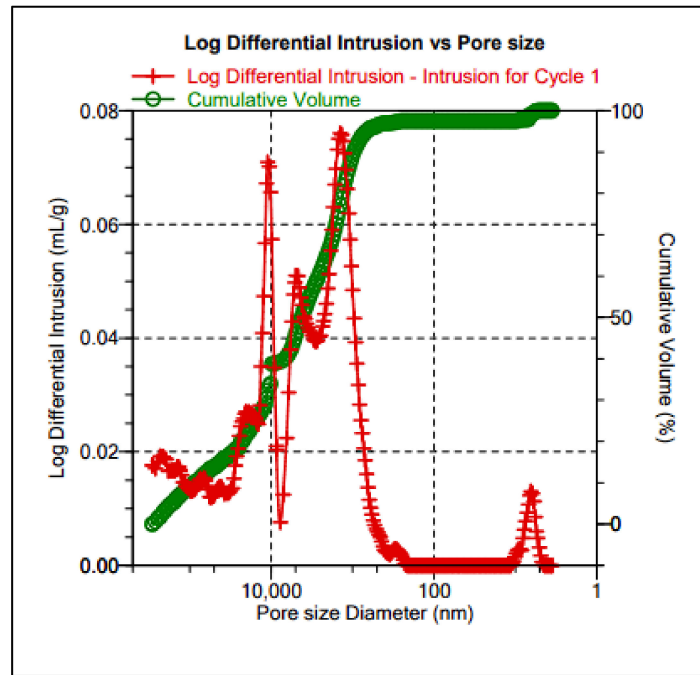


Figure 13. Pore size distribution of full 3D-printed cylinders determined using mercury intrusion porosimetry.

Truxova et al. [40] characterized FFF-manufactured Al₂O₃ samples using filaments produced by Zetamix (Nanoe, France) with 52 vol.% of Al₂O₃ and a polyolefin-based binder, utilizing a chemical pre-debinding step. According to their results, the average mass loss during chemical and thermal treatment was 22.6 mass% and average shrinkage of the specimens, 22.5%. Due to the fact that in the present research lightweight polymers were used, the mass loss is considerably lower. Furthermore, Truxova et al. managed to manufacture rectangular specimens with a total porosity of the sintered body of 0.46%. In order to be applicable in the field of refractories, steel-casting nozzles have to obtain much higher values, since a micropore network impedes crack propagation during thermal shock.

3.6. Hot-Stage Microscope Test

Sintered nozzles were intended for a static corrosion test in contact with molten steel alloy at 1600 °C in a hot-stage microscope. After the test, the nozzle was cut in half and its cross-section was analysed for any corrosion reaction using SEM/EDS. The analysis of the internal surface of the nozzle with LSM and SEM/EDS is shown in Figure 14. Position II represents the zone that was in contact with steel melt, whereas position I, at the interphase. No Fe could be detected at position I (Table 9), which indicates no melt intrusion into the wall of the nozzle. The only element that diffused inside the nozzle wall was Cr, at a depth of approx. 1 mm.

Table 9. Results of EDS analysis corresponding with scans indicated in Figure 14.

	O	Na	Mg	Al	Ca	Si	Cr	Fe
Scan I	52.4	0.3	9.5	33.4	-	2.6	1.8	-
Scan II	60.6	-	8.9	28.3	0.2	-	1.4	0.6

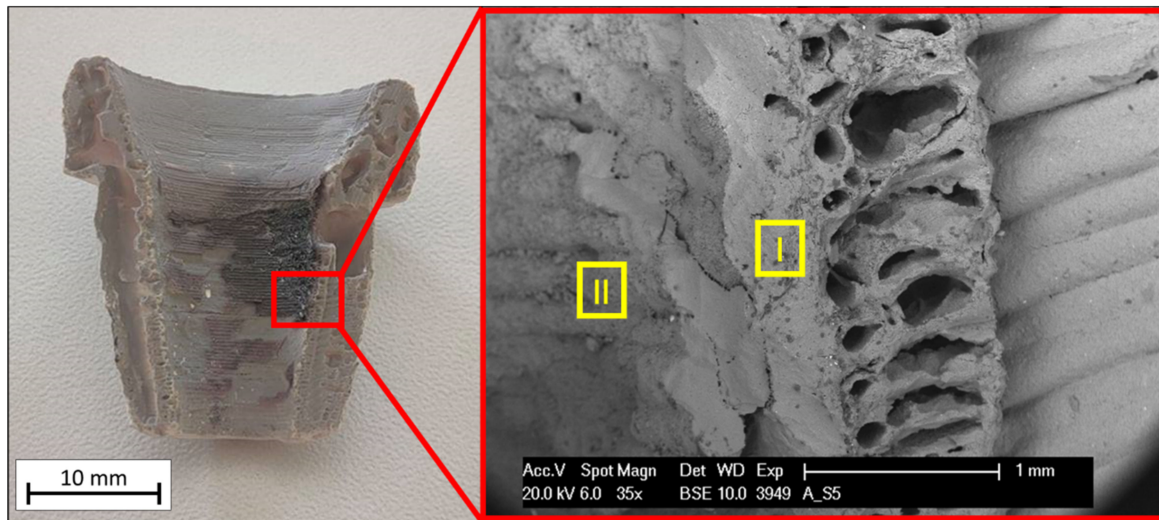


Figure 14. LSM image (left) and SEM micrograph (right) of the nozzle after contact with 316L stainless steel (regions of interests with performed EDS scans I and II are marked in yellow).

3.7. Steel-Casting Simulator Test

The preheated nozzle (approx. 800 °C) was loaded with 100 kg of steel melt (1600 °C) for 4 min (Figure 15).

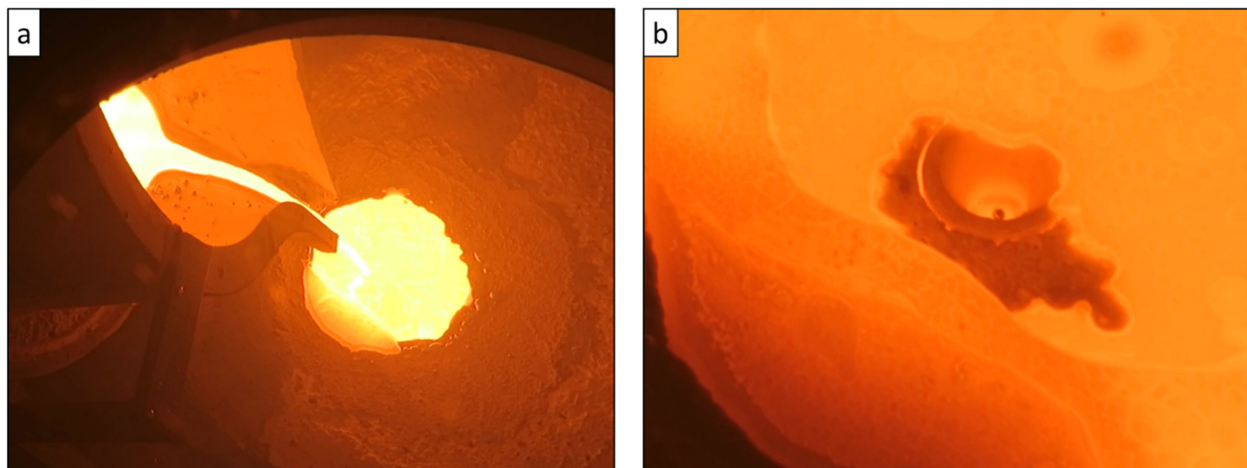


Figure 15. Steel-casting simulator test: (a) 100 kg of steel being poured through the 3D-printed nozzle, (b) proof of the feasibility.

The rapidly heating thermal gradient on the surface of the top of the nozzle at the moment of contact with steel melt was approximately 800 K (from 800 °C to 1600 °C). More so, pouring steel melt also caused mechanical loading of the nozzle. However, our 3D-printed, fine-grained, alumina-rich spinel-based nozzle with tailored infill structure withstood the thermomechanical loading for the whole casting time. The nozzle remained fully operable throughout the whole experiment and revealed no damage due to thermal shock or corrosive reactions (Figure 16). It is remarkable that the nozzle also survived the cooling to room temperature after the steel was poured, since during the cooling process, high tensile stresses occur on the outer surface of the nozzle.

After the steel-casting test, the nozzle was exposed to CT analysis; however, no intrusion of steel was detected, and no cracks in the resolution range of the CT could be registered. Such promising results indicate that with combination of AM technologies and tailor-made inner geometry (layered thin outer walls and macro-cavities) it is possible to

manufacture industrially applicable ceramic refractories that survive both mechanical load and thermal shock caused by steel melt.

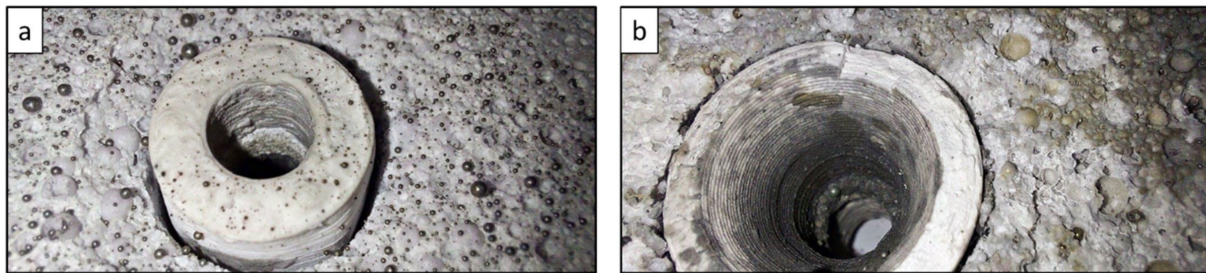


Figure 16. Nozzle after steel-casting simulator test: (a) bottom part of the nozzle, (b) upper part of the nozzle.

This research represents thermal treatment routes for AR78-based ceramic refractory parts of pre-defined geometry. Naturally, in order to scale up to larger 3D-printed bodies using the same material, both debinding and sintering routes should be readjusted in order to ensure the full removal of binder material as well as proper sintering of the part. Such binder composition might also be utilized to manufacture metal–ceramic composite parts; however, in this case, due to the possibly higher density of solid load of the filament, the composition of the filament material also needs readjustment, i.e., a lower solid load of the filament material as well as a different volumetric ratio of backbone cellulose to thermoplastic polyethylene. It is also to be mentioned that composite materials might need additional doping to equalize the sintering temperatures of the composite parts. During the experiments, it was noticed that the particle size distribution of the solid phase affects the debinding process. A bi-modal distribution that caused dense packing of the AR78 powder prevented the binder material from evaporating properly, causing eruption/explosion of the outer walls of the printed parts.

4. Conclusions

The development of filaments based on spinel fine ceramics ready to use in FFF 3D-printing technologies has been explored. The developed filaments show exceptional form-stability at elevated temperatures during debinding and sintering. Adapted filament binder composition allowed us to eliminate the solvent chemical pre-debinding step indispensable for other technologies and achieve successful results using only thermal debinding, which significantly lowers the price and time of manufacture. The debinding and sintering curves were determined with thermal analyses and filament stability tests and led to debinding steps at different temperatures ensuring consecutive removal of the respective binder ingredients.

According to mercury porosimetry tests, the open porosity of the printed samples was 21.5 vol%, with pore sizes less than 30 μm , which are not infiltrated by steel melt in the case of a non-wetting material such as spinel in contact with steel melt. The FFF-generated macro- and micro-structure of fine-grained alumina-rich spinel, combining (a) a layer-by-layer microstructure development with (b) tailored macro-cavities, lead to carbon-free ceramic components with an outstanding thermal-shock performance. The 3D-printed components based on fine-grained spinel can be used as nozzles, stoppers, or other functional components during casting of metal melts.

Further research might be focused on utilization of the developed filament binder–plasticizer system for multi-material composite applications, such as metal/ceramic composites, i.e., for non-ferrous metallurgy applications and/or electro-chemical applications.

5. Patents

There are two German patent applications resulting from the work reported in this manuscript:

German patent application DE 10 2022 001 071.5, application date: 29 March 2022 (Inventors: Aneziris, C.G., Malczyk, P., Yaroshevskiy, S., Dudczig, S., Hubálková, J.)

German patent application DE 10 2022 001 070.4, application date: 29 March 2022 (Inventors: Aneziris, C.G., Yaroshevskiy, S., Malczyk, P.)

Author Contributions: Conceptualization, C.G.A., P.M., S.Y. and C.W.; methodology, P.M., C.W. and U.L.; software, P.M.; validation, C.G.A., S.Y. and P.M.; formal analysis, S.Y.; investigation, S.Y., P.M. and S.D.; data curation, S.Y.; writing—original draft preparation, S.Y. and C.G.A.; writing—review and editing, P.M. and J.H.; visualization, J.H.; supervision, C.G.A.; funding acquisition, C.G.A. and U.L. All authors have read and agreed to the published version of the manuscript.

Funding: This research was funded by the German Federal Ministry of Economic Affairs and Climate Action, grant number ZF 4096916 AG8.

Institutional Review Board Statement: Not applicable.

Informed Consent Statement: Not applicable.

Data Availability Statement: The data that support the findings of this study are available from the corresponding author upon reasonable request.

Acknowledgments: The authors would like to thank G. Schmidt and C. Ludewig for help with calorimetry analysis as well as R. Fricke and R. Kaulfürst for technical support.

Conflicts of Interest: The authors declare no conflict of interest. The funders had no role in the design of the study; in the collection, analyses, or interpretation of data; in the writing of the manuscript; or in the decision to publish the results.

References

1. Saâdaoui, M.; Chevalier, J.; Fantozzi, G. Thermal Shock and Thermal Fatigue of Alumina Ceramics. In *Fracture Mechanics of Ceramics*; Springer: Boston, MA, USA, 2002. [\[CrossRef\]](#)
2. Luo, M.; Li, Y.; Jin, S.; Sang, S.; Zhao, L.; Wang, Q.; Li, Y. Microstructure and mechanical properties of multi-walled carbon nanotubes containing Al₂O₃-C refractories with addition of polycarbosilane. *Ceram. Int.* **2013**, *39*, 4831–4838. [\[CrossRef\]](#)
3. Zhang, L.; Wang, Y.; Zuo, X. Flow Transport and Inclusion Motion in Steel Continuous-Casting Mold under Submerged Entry Nozzle Clogging Condition. *Metall. Mater. Trans. B* **2008**, *39*, 534–550. [\[CrossRef\]](#)
4. Vermeulen, Y.; Coletti, B.; Blanpain, B.; Wollants, P.; Vleugels, J. Material Evaluation to Prevent Nozzle Clogging during Continuous Casting of Al Killed Steels. *ISIJ Int.* **2002**, *42*, 1234–1240. [\[CrossRef\]](#)
5. Henneberg, D.; Ricoeur, A.; Judt, P. Multiscale modeling for the simulation of damage processes at refractory materials under thermal shock. *Comput. Mater. Sci.* **2013**, *70*, 187–195. [\[CrossRef\]](#)
6. Kim, G.E. *Thermal Sprayed Nano-Structured Coatings: Applications and Developments in Nanostructured Materials: Processing, Properties and Applications*, 2nd ed.; William Andrew: Norwich, NY, USA, 2007; pp. 91–118.
7. Bradt, R.C.; Harmuth, H. The Fracture Resistance of Refractories. *Refract. Worldforum* **2011**, *3*, 129–135.
8. Brochen, E.; Clasen, S.; Dahlem, E.; Dannert, C. Determination of the thermal shock resistance of refractories. *Refract. Worldforum: Manuf. Perform. High Temp. Mater.* **2016**, *8*, 1.
9. Brochen, E.; Pötschke, J.; Aneziris, C.G. Improved Thermal Stress Resistance Parameters Considering Temperature Gradients for Bricks in Refractory Linings. *Int. J. Appl. Ceram. Technol.* **2014**, *11*, 371–383. [\[CrossRef\]](#)
10. Skiera, E.; Malzbender, J.; Mönch, J.; Dudczig, S.; Aneziris, C.G.; Steinbrech, R.W. Controlled Crack Propagation Experiments with a Novel Alumina-Based Refractory. *Adv. Eng. Mater.* **2012**, *14*, 248–254. [\[CrossRef\]](#)
11. Aksel, C.; Warren, P.D. Thermal shock parameters [R, R''' and R'''''] of magnesia–spinel composites. *J. Eur. Ceram. Soc.* **2003**, *23*, 301–308. [\[CrossRef\]](#)
12. Habib, K.A.; Saura, J.J.; Ferrer, C.; Damra, M.S.; Giménez, E.; Cabedo, L. Comparison of flame sprayed Al₂O₃/TiO₂ coatings: Their microstructure, mechanical properties and tribology behavior. *Surf. Coat. Technol.* **2006**, *201*, 1436–1443. [\[CrossRef\]](#)
13. Belghalem, H.; Hamidouche, M.; Gremillard, L.; Bonnefont, G.; Fantozzi, G. Thermal shock resistance of two micro-structured alumina obtained by natural sintering and SPS. *Ceram. Int.* **2014**, *40*, 619–627. [\[CrossRef\]](#)
14. Abel, J.; Scheithauer, U.; Janics, T.; Hampel, S.; Cano, S.; Müller-Köhn, A.; Günther, A.; Kukla, C.; Moritz, T. Fused Filament Fabrication (FFF) of Metal-Ceramic Components. *J. Vis. Exp.* **2019**, *143*, e57693. [\[CrossRef\]](#)
15. Schwarzer, E.; Götz, M.; Markova, D.; Stafford, D.; Scheithauer, U.; Moritz, T. Lithography-based ceramic manufacturing (LCM)—Viscosity and cleaning as two quality influencing steps in the process chain of printing green parts. *J. Eur. Ceram. Soc.* **2017**, *37*, 5329–5338. [\[CrossRef\]](#)
16. Scheithauer, U.; Schwarzer, E.; Richter, H.J.; Moritz, T. Thermoplastic 3D Printing—An Additive Manufacturing Method for Producing Dense Ceramics. *J. Appl. Ceram. Technol.* **2014**, *12*, 26–31. [\[CrossRef\]](#)

17. Paolini, A.; Kollmannsberger, S.; Rank, E. Additive manufacturing in construction: A review on processes, applications, and digital planning methods. *Addit. Manuf.* **2019**, *30*, 100894. [[CrossRef](#)]
18. Tempelman, E.; Shercliff, H.; Ninaber van Eyben, B. Additive Manufacturing. In *Manufacturing and Design—Understanding the Principles of How Things Are Made*, 1st ed.; Butterworth-Heinemann: Oxford, UK, 2014; pp. 187–200.
19. Clemens, F.; Schulz, J.; Gorjan, L.; Liersch, A.; Sebastian, T.; Sarraf, F. Debinding and Sintering of Dense Ceramic Structures Made with Fused Deposition Modeling. In *Industrializing Additive Manufacturing: Proceedings of AMPA2020*; Springer: Berlin/Heidelberg, Germany, 2021; pp. 293–303. [[CrossRef](#)]
20. Pejak Simunec, D.; Sola, A. Emerging Research in Conductive Materials for Fused Filament Fabrication: A Critical Review. *Adv. Eng. Mater.* **2022**, *24*, 2101476. [[CrossRef](#)]
21. Gehre, P.; Aneziris, C.G. EBSD- and CT-analyses for phase evolution and crack investigations of thermal shocked flame sprayed alumina and alumina-rich structures. *Ceram. Int.* **2011**, *37*, 1731–1737. [[CrossRef](#)]
22. Kaczmarek, R.; Dupre, J.; Doumalin, P.; Pop, O.; Breder-Teixeira, L.; Gillibert, J.; Blond, E.; Huger, M. Thermomechanical behaviour of an alumina spinel refractory for steel ladle applications. In Proceedings of the XVI ECerS CONFERENCE 2019 Torino, Turin, Italy, 16 June 2019. [[CrossRef](#)]
23. Li, H.; Liu, Y.; Liu, Y.; Hu, K.; Lu, Z.; Liang, J. Effects of Solvent Debinding on the Microstructure and Properties of 3D-Printed Alumina Ceramics. *ACS Omega* **2020**, *5*, 27455–27462. [[CrossRef](#)]
24. Scheithauer, U.; Slawik, T.; Schwarzer, E.; Richter, H.-J.; Moritz, T.; Michaelis, A. Additive Manufacturing of Metal-Ceramic-Composites by Thermoplastic 3D-Printing (3DTP). *J. Ceram. Sci. Technol.* **2015**, *6*, 125–132. [[CrossRef](#)]
25. Brecher, C.; Emonts, M.; Dubratz, M.; Kermer-Meyer, A. Automated Manufacturing of Fiber-Reinforced Thermoplastic 3D-Lightweight Components. In *Future Trends in Production Engineering: Proceedings of the First Conference of the German Academic Society for Production Engineering (WGP), Berlin, Germany, 8–9 June 2011*; Springer: Berlin/Heidelberg, Germany, 2013; pp. 153–160. [[CrossRef](#)]
26. Mamatha, S.; Biswas, P.; Ramavath, P.; Das, D.; Johnson, R. 3D printing of complex shaped alumina parts. *Ceram. Int.* **2018**, *44*, 19278–19281. [[CrossRef](#)]
27. Wang, X.; Jiang, M.; Zhou, Z.; Gou, J.; Hui, D. 3D printing of polymer matrix composites: A review and prospective. *Compos. Part B Eng.* **2017**, *110*, 442–458. [[CrossRef](#)]
28. Gosselin, C.; Duballet, R.; Roux, P.h.; Gaudillière, N.; Dirrenberger, J.; Morel, P.H. Large-scale 3D printing of ultra-high performance concrete—A new processing route for architects and builders. *Mater. Des.* **2016**, *100*, 102–109. [[CrossRef](#)]
29. Dizon, J.R.C.; Espera, A.H.; Chen, Q.; Advincula, R.C. Mechanical characterization of 3D-printed polymers. *Addit. Manuf.* **2018**, *20*, 44–67. [[CrossRef](#)]
30. Nötzel, D.; Eickhoff, R.; Hanemann, T. Fused Filament Fabrication of Small Ceramic Components. *Materials* **2018**, *11*, 1463. [[CrossRef](#)]
31. Orlovská, M.; Chlup, Z.; Bača, L.; Janek, M.; Kitzmantel, M. Fracture and mechanical properties of lightweight alumina ceramics prepared by fused filament fabrication. *J. Eur. Ceram. Soc.* **2020**, *40*, 4837–4843. [[CrossRef](#)]
32. Vozárová, M.; Neubauer, E.; Bača, L.; Kitzmantel, M.; Feranc, J.; Trembošová, V.; Peciar, P.; Kritikos, M.; Orlovská, M.; Janek, M.; et al. Preparation of fully dense boron carbide ceramics by Fused Filament Fabrication (FFF). *J. Eur. Ceram. Soc.* **2022**, *43*, 1751–1761. [[CrossRef](#)]
33. Dudczig, S.; Aneziris, C.G.; Ballaschk, U. Testing of Thermal Shock Resistant Fine Grained Alumina Ceramics in a Metal Casting Simulator. *Refract. Worldforum* **2012**, *4*, 105–111.
34. Li, D.; Zhou, L.; Wang, X.; He, L.; Yang, X. Effect of Crystallinity of Polyethylene with Different Densities on Breakdown Strength and Conductance Property. *Materials* **2019**, *12*, 1746. [[CrossRef](#)]
35. Greene, J.P. Microstructures of Polymers. In *Automotive Plastics and Composites—Materials and Processing*, 1st ed.; William Andrew: Oxford, UK, 2021; pp. 27–37.
36. Nötzel, D.; Hanemann, T. New Feedstock System for Fused Filament Fabrication of Sintered Alumina Parts. *Materials* **2020**, *13*, 4461. [[CrossRef](#)]
37. Schafföner, S.; Dietze, C.; Möhmel, S.; Fruhstorfer, J.; Aneziris, C.G. Refractories containing fused and sintered alumina aggregates: Investigations on processing, particle size distribution and particle morphology. *Ceram. Int.* **2017**, *43*, 4252–4262. [[CrossRef](#)]
38. Lube, T.; Staudacher, M.; Hofer, A.; Schlacher, J.; Bermejo, R. Stereolithographic 3D Printing of Ceramics: Challenges and Opportunities for Structural Integrity. *Adv. Eng. Mater.* **2022**, 2200520. [[CrossRef](#)]
39. Routschka, G. *Anhang in Taschenbuch Feuerfeste Werkstoffe*, 3rd ed.; Vulkan-verlag: Essen, Germany, 2001; p. 428.
40. Truxová, V.; Šafka, J.; Sobotka, J.; Macháček, J.; Ackermann, M. Alumina Manufactured by Fused Filament Fabrication: A Comprehensive Study of Mechanical Properties and Porosity. *Polymers* **2022**, *14*, 991. [[CrossRef](#)]

Disclaimer/Publisher's Note: The statements, opinions and data contained in all publications are solely those of the individual author(s) and contributor(s) and not of MDPI and/or the editor(s). MDPI and/or the editor(s) disclaim responsibility for any injury to people or property resulting from any ideas, methods, instructions or products referred to in the content.